Advanced Powder Materials 1 (2022) 100058

Contents lists available at ScienceDirect

Advanced Powder Materials

journal homepage: www.keaipublishing.com/en/journals/advanced-powder-materials

Single-atom zinc catalyst for co-production of hydrogen and fine chemicals in soluble biomass solution

Jiliang Ma [a], Xinze Li [a], Yancong Li [a], Gaojie Jiao [a], Hang Su [b], Dequan Xiao [b,***], Shangru Zhai [a,**], Runcang Sun [a,*]

[a] Liaoning Key Lab of Lignocellulose Chemistry and BioMaterials, Liaoning Collaborative Innovation Center for Lignocellulosic Biorefinery, College of Light Industry and Chemical Engineering, Dalian Polytechnic University, Dalian, 116034, China

[b] Center for Integrative Materials Discovery, Department of Chemistry and Chemical Engineering, University of New Haven, 300 Boston Post Rd, West Haven, CT, 06516, United States

ARTICLE INFO

Keywords:
Biorefinery
Single-atom photocatalyst
Photocatalysis
Hydrogen
Co-production

ABSTRACT

Single-atom photocatalysts (SAPCs) have attracted great interests due to their remarkable atom utilization efficiency, excellent activity, and selectivity, yet no application in synchronous biorefinery and water splitting. Here, efficient SAPCs based on atomically dispersed Zn atoms on carbon nitride (named Zn−mCN) were produced. Experiments verified that Zn−mCN has widened adsorption range of visible-light and lowered ability of electron−hole recombination, leading to excellent photocatalytic redox activity for synchronous biorefinery and water splitting to co-produce lactic acid (selectivity up to 91.0%) and hydrogen (~15898.8 μmol g^{-1} h^{-1}). This system has excellent universality for small- molecule monosaccharides and macromolecular xylan. Poisoning experiments showed that h^+, $^1O_2$, $\cdot O_2^-$ and ·OH can promote the simultaneous production of lactic acid and hydrogen. This work realized full utilization of whole redox reaction and provided a novel strategy for efficient and concomitant production of hydrogen and value-added chemicals from biomass-derived feedstocks aqueous solutions.

1. Introduction

Photo-reforming of biomass-derived feedstocks into value-added chemicals offers a promising strategy to solve the limited energy reserves and environmental pollution derived from fossil fuels [1–5]. However, the complex structure and multifarious functional groups in biomass demand excellent photocatalysts to simultaneously meet three criteria, i.e., high activity, selectivity and stability [6–8]. Furthermore, the environment economic efficiency of the entire system is an important factor that constrains the development of photocatalysis in biorefinery. However, photocatalytic selective oxidation of biomass only uses the oxidation half-reaction in the entire redox system, which severely limits the economic benefits of the whole reaction system. On the contrary, photocatalytic water splitting to hydrogen only uses the half-reduction reaction of the entire reaction system, and the conversion of sacrificial agents is not further investigated. For example, Wakerley et al. [9] developed a CdS quantum dots photocatalytic system for hydrogen production via reforming of cellulose, hemicellulose and lignin in alkaline aqueous solution. However, no further study of oxidation half-reaction was explored. Therefore, co-production of value-added chemicals and hydrogen in one system is a great challenge. In 2016, Zhang et al. [10] developed a novel photocatalytic system for co-production of sugars, CO_2 in the oxidation half-reaction and hydrogen in the reduction half-reaction via reforming of cellulose. This reported system achieved hydrogen release without additional sacrificial agents, meanwhile, provided a novel strategy for production of sugars and liquid fuels. Unfortunately, the universality of the reaction system was not explored, limiting its practical application. Overall, the key to obtaining an efficient, environmentally friendly, and inexpensive photocatalytic system for co-production of hydrogen and fine chemicals is to develop a novel photocatalyst. Single-atom catalysts [11], particularly here single-atom photocatalysts (SAPCs) with maximum atom-utilization efficiency, fully exposed and evenly distributed active sites, as well as excellent selectivity [12–20], provide a great opportunity to tackle these

* Corresponding author.
** Corresponding author.
*** Corresponding author.
E-mail addresses: dxiao@newhaven.edu (D. Xiao), zhaisr@dlpu.edu.cn (S. Zhai), rcsun3@dlpu.edu.cn (R. Sun).

https://doi.org/10.1016/j.apmate.2022.100058
Received 21 March 2022; Received in revised form 7 May 2022; Accepted 9 May 2022
Available online 14 May 2022

challenges in synchronous biorefinery and water splitting to produce value-added chemicals and hydrogen. However, the high surface free energy of single atoms leads to difficult preparation of single-atom catalysts with high contents [21,22], until recently, high dispersion of single-atom in catalysts has gradually attracted great interests due to their remarkable atom economy, excellent activity and selectivity, yet limited success has been achieved. Meanwhile, the application of single-atom photocatalyst in synchronous biorefinery and hydrogen release is rarely reported. Thus, developing efficient, environmentally friendly and economical SAPCs for simultaneously photocatalytic biorefinery and water splitting is essential.

Zinc (Zn) is an abundant element on earth, and its development and utilization have attracted more and more interest, especially Zn single-atoms catalyst. One reason is that the d orbitals of Zn are filled with electrons [23], and the other is that the Gibbs free energy of *Zn in Zn–N_4 is high [24], leading to high activity and stability. Functional carbon nitride material plays a crucial role in catalysis, owing to its non-expensive raw material, simple and environmental process, as well as high activity [25–33]. However, pure carbon nitride suffered from limited photo-absorption region and high recombination rate of photo-induced carriers, resulting in low photocatalytic activity [34]. Interestingly, the Zn−N_x structure can be formed by merging of them, and the merit of Zn single atoms is the complement of carbon nitride. The organic combination of the two will improve their practical application from many aspects, such as economy, environmental protection, stability and efficiency, especially in the photocatalytic biorefinery. However, few such SAPCs have been synthesized and used in the field of synchronous biorefinery and water splitting up to now.

Here, we developed a novel calcination−calcination−washing (CCW) strategy to prepare Zn single-atom on carbon nitride. The CCW strategy can simply control the dispersion and content of Zn single-atom. Moreover, the building of Zn–N_6 structure in Zn−mCN obviously broadened the absorption range of visible-light, and reduced the photoluminescence strength, leading to enhanced photocatalytic performance. In addition, the atomically dispersed Zn on carbon nitride exhibits remarkable redox activity for photocatalytic biomass-derived pentoses and hexoses to value-added chemicals and hydrogen. This work provides a potential for synchronous biorefinery and water splitting via photocatalysis.

2. Experimental section

2.1. Materials

Melamine, zinc chloride ($ZnCl_2$), potassium hydroxide (KOH), xylose, glucose, fructose and xylan were provided by Macklin Industrial Corporation (Shanghai, China). Hydrochloric acid (HCl), benzoquinone (BQ), potassium iodide (KI), isopropanol (IPA), tryptophan (Trp) and other reagents were obtained from Dalian Chemical Reagent Factory, China. All chemicals were of analytic grade and used directly without further purification.

2.2. Preparation of CN

In a typical procedure, a certain amount of melamine was added into the HCl solution (0.5 mol/L), and the obtained slurry was directly calcinated at 400 °C for 2 h under the air condition. The obtained CN precursor was ground thoroughly and then calcinated at 560 °C for 2 h to give CN sample.

2.3. Preparation of Zn−mCN

Initially, a certain amount of $ZnCl_2$ was added into the HCl solution (0.5 mol/L) under the condition of continuous stirring in a beaker. When $ZnCl_2$ was dissolved, a certain amount of melamine was added into the mixed solution with violent agitation for 60 min. The obtained slurry was directly transferred to the tube furnace, and the tube furnace was then heated to 400 °C for 2 h under the air atmosphere. Then, the products were ground thoroughly and heated to 560 °C for another 2 h. The final products were sonicated for 5 min and then washed with deionized water until the filtrate became neutral, and finally dried at 100 °C for 12 h to give Zn−mCN photocatalyst.

2.4. Photocatalytic synchronous biorefinery and water splitting to high-value chemicals

In a typical procedure, 300 mg of xylose and a certain amount of Zn−mCN and $H_2PtCl_6{\cdot}6H_2O$ were added into 30 mL of KOH solution with different concentrations. The mixed system was sonicated for 5 min

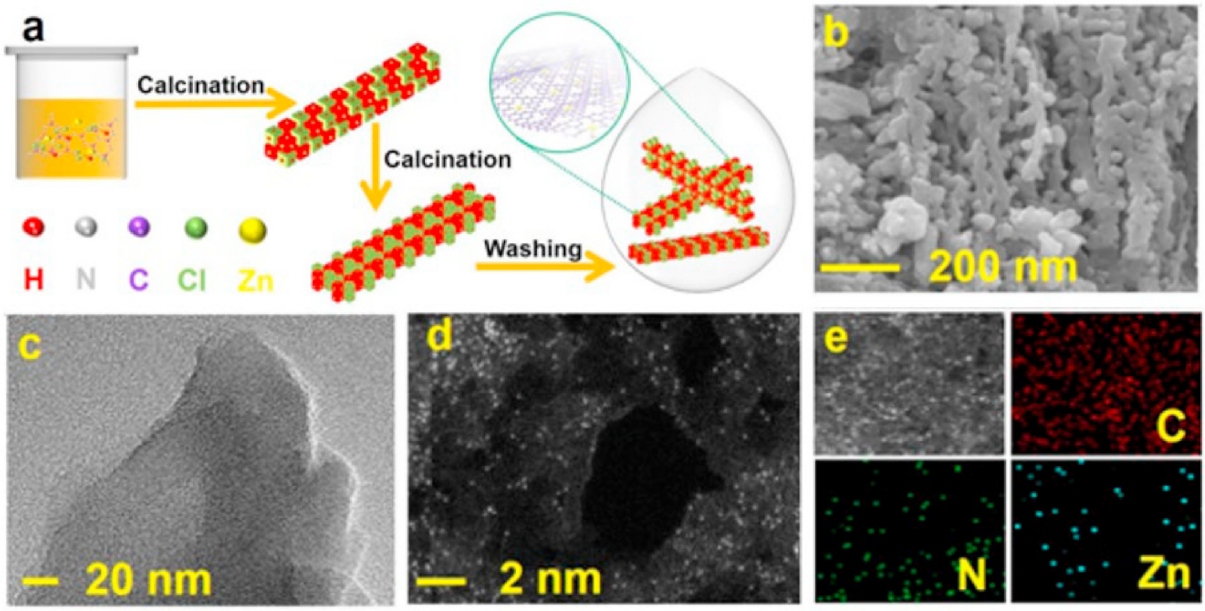

Fig. 1. Synthesis and structural characterizations of single-atom Zn−mCN photocatalysts: (a) Schematic illustration for synthesis; (b) SEM image; (c) TEM image; (d) AC HAADF-STEM image; (e) HAADF-STEM image and corresponding EDX element mapping.

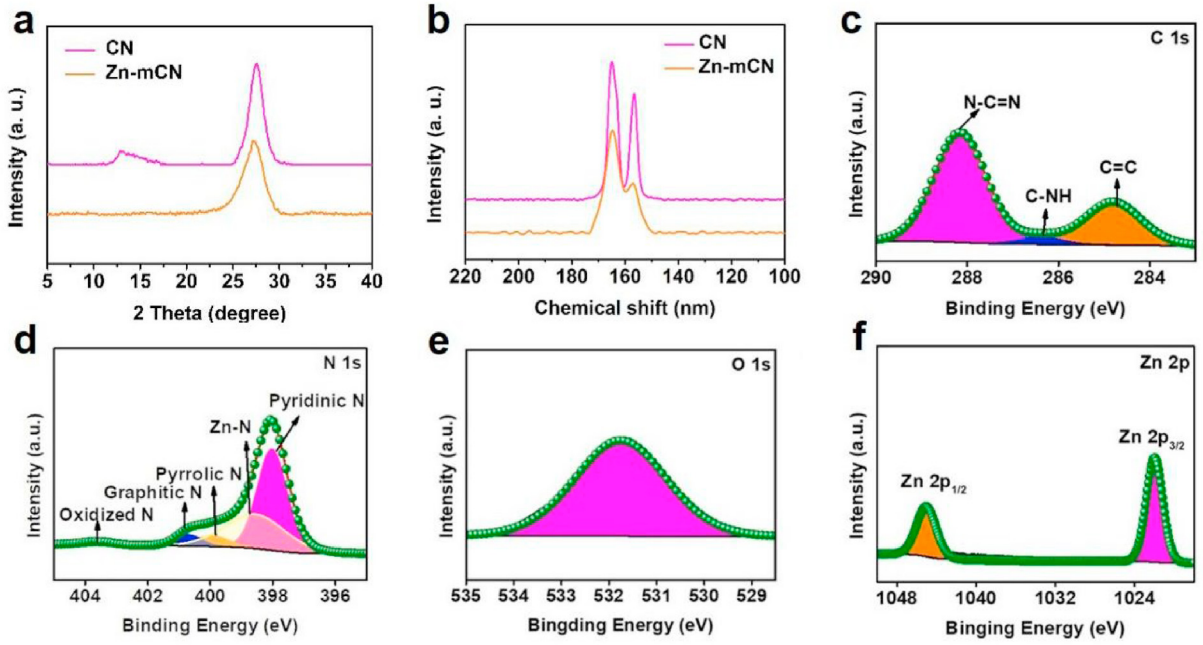

Fig. 2. XRD patterns (a) and solid-state ^{13}C NMR profiles (b) of CN and Zn−mCN. XPS spectra of Zn−mCN: C 1s (c); N 1s (d); O 1s (e); Zn 2p (f).

and then filled with Ar (101 kPa). Finally, the obtained system was reacted at 30 °C for a period of time in the presence of visible light (VLight 10 W, 360–780 nm). When the reaction was completed, the hydrogen release was detected by gas chromatography (GC7900) equipped with TCD detector at 100 °C (Column pressure: 25 psi, column temperature: 50 °C, carrier gas: Ar, current: 50 mA, sample meter temperature: 100 °C) while the liquid products were then filtrated and detected by high-performance liquid chromatography (HPLC).

2.5. Universality test

Typically, 300 mg of various biomass-derived sugars (e.g., xylose, arabinose, glucose, fructose, rhamnose, mannose), 100 mg of Zn−mCN, and 300 μL of $H_2PtCl_6{\cdot}6H_2O$ (6.5 mmol/L) were added into 30 mL of KOH solutions (7.0 mol/L). The obtained systems were sonicated for 5 min and then filled with Ar (101 kPa). Finally, these systems were performed at 30 °C for 5 h in the presence of visible light (10 W). Once these reactions were completed, the hydrogen release was detected by gas chromatography (GC7900), while the liquid products were then filtrated and detected by HPLC.

2.6. Poisoning experiment

To investigate the effects of different oxidative active species on the photocatalytic synchronous xylose conversion and water splitting to lactic acid and hydrogen, a series of experiments were performed. Typically, 100 mg of Zn−mCN, 300 mg of xylose, 300 μL of $H_2PtCl_6{\cdot}6H_2O$ (6.5 mmol/L) and 0.05 mol sacrificial agents (e.g., BQ, KI, IPA, Trp) were added into 30 mL of KOH solutions (7.0 mol/L). The mixtures were sonicated for 5 min and then filled with Ar (101 kPa). Finally, the obtained systems were performed at 30 °C for 5 h irradiated by 10 W visible light. Once these reactions were completed, the hydrogen release was detected by gas chromatography (GC7900) while the conversion of xylose and the yield of lactic acid were detected by HPLC.

2.7. Recycling test

To explore the reusability of Zn−mCN, a series of experiments were carried out. In a typical procedure, 100 mg of Zn−mCN and 300 mg of xylose as well as 300 μL of $H_2PtCl_6{\cdot}6H_2O$ (6.5 mmol/L) were added into 30 mL of KOH solutions (7.0 mol/L). The mixture was sonicated for 5 min and then filled with Ar (101 kPa). The obtained reaction system was performed at 30 °C for 5 h irradiated by 10 W visible light. Once these reactions were completed, the hydrogen release was detected by gas chromatography (GC7900), while the conversion of xylose and the yield of lactic acid were detected by HPLC. Finally, the solid was washed with deionized water several times until the filtrate became neutral. The Zn−mCN was dried at 100 °C for 12 h prior to reuse.

3. Results and discussion

3.1. Catalyst preparation and characterization

The preparation process of Zn−mCN photocatalysts is shown in Fig. 1a. Initially, $ZnCl_2$ as Zn source was dissolved in HCl solution (0.5 mol/L). Melamine was added into the solution to form a uniform mixture of melamine salt and $ZnCl_2$. Subsequently, the mixture was calcinated at 400 °C for 2 h under air conditions to give the precursor of Zn−mCN. The precursor was ground thoroughly and then calcinated at 560 °C for 2 h. The Zn−mCN photocatalysts were obtained by washing with deionized water until the filtrate was neutral. In this synthetic strategy, the volatilization of HCl inhibited the construction of Zn—Zn bond during the CCW processes. By regulating the $ZnCl_2$ dosage, the loading capacity of single-atom Zn is increased from 5.5 wt.% to 14.1 wt.% (Table S1).

To investigate the morphology of Zn−mCN, scanning electron microscopy (SEM) and transmission electron microscopy (TEM) were performed. Figs. 1b and S1 show the three-dimensional structure of Zn−mCN. High-resolution TEM (HRTEM) image indicates that no apparent Zn nanoparticles were observed (Figs. 1c and S2). Interestingly, a series of isolated bright spots were observed in the matrix of Zn−mCN via aberration-corrected HAADF-STEM (AC HAADF-STEM) technique with sub-angstrom resolution, suggesting that atomic dispersion of Zn was doped in Zn−mCN (Fig. 1d and e and S3). The C, N and Zn mappings of Zn−mCN by electron energy-loss spectroscopy (EELS) demonstrate that the Zn atoms are evenly distributed on the catalyst surface (Fig. 1e).

For XRD patterns, Zn−mCN exhibits a similar crystalline structure to graphitic carbon nitride (JCPDS Card No. 87–1526), and no additional peaks associated with other Zn species were detected (Fig. 2a). This finding shows that Zn atoms are highly dispersed in Zn−mCN, which coincides with the TEM results. Meanwhile, with the Zn-loading in the

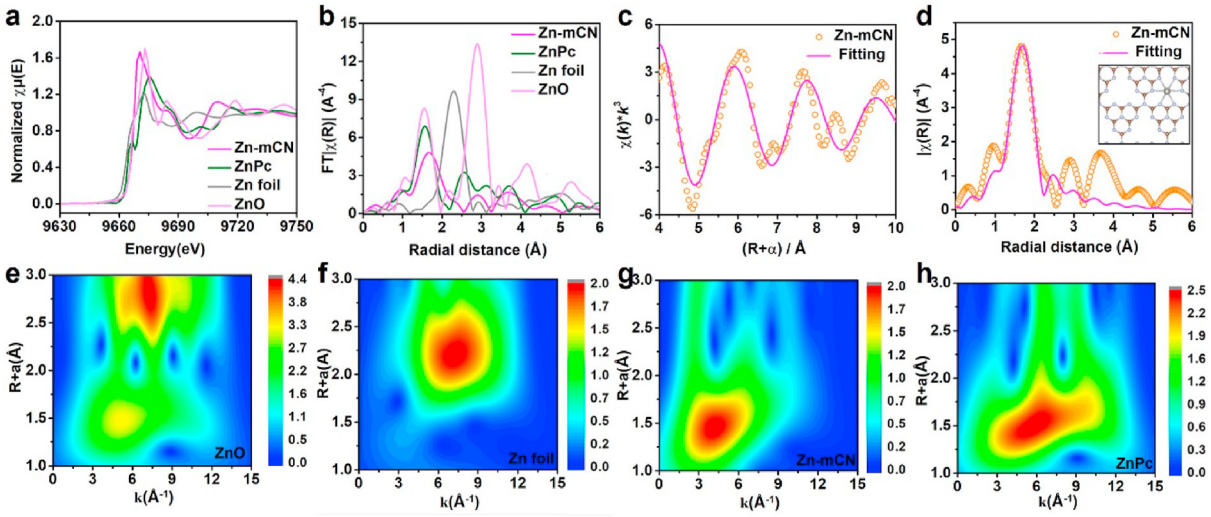

Fig. 3. (a) XANES spectra at Zn K-edge of Zn−mCN, Zn foil, ZnO and ZnPc. (b) Fourier transform (FT) at Zn K-edge of Zn−mCN, Zn foil, ZnO and ZnPc. (c) Corresponding EXAFS fitting curves of Zn−mCN at k space. (d) Corresponding EXAFS fitting curves of Zn−mCN at R space, inset is the schematic structure model of Zn−mCN, Zn (gray), N (light blue), C (brown). (e–h) Wavelet transform (WT) of ZnO, Zn foil, Zn−mCN and ZnPc, respectively.

framework of CN, the intensity of (100) peak was gradually decreased. Furthermore, ^{13}C NMR profiles indicated the presence of tri-s-triazine units in the CN and Zn−mCN (Fig. 2b) [35]. To investigate the chemical status of Zn−mCN, the XPS spectra were performed. The spectrum confirms that the existence of C, N, O, Zn in Zn−mCN (Fig. S4). For C 1s spectrum, three peaks were observed at 288.2, 286.2, and 284.8 eV, corresponding to N—C═N, C—NH, and C═C (Fig. 2c), respectively [36]. As shown in Fig. 2d, the N 1s spectra gave five peaks at 404.0, 401.2, 400.4, 399.0, and 398.5 eV, which are attributed to the oxidized N, graphitic N, pyrrolic N, Zn–N, and pyridinic N, respectively [22,37]. Here, the N 1s of CN was also performed. As shown in Fig. S5, it can be found that N defects in the Zn−mCN allow electrons to escape, and after the formation of Zn—N bonds, the electrons are transferred from N atoms to Zn atoms to maintain equilibrium [38]. The O 1s at 531.8 eV is originated from N—C—O corresponding to lattice oxygen in the photocatalyst (Fig. 2e) [39]. For Zn 2p spectra (Fig. 2f), two peaks at 1022.0 and 1045.0 eV belong to the Zn $2p_{3/2}$ and Zn $2p_{1/2}$ electronic states of Zn^{2+} [40].

To further investigate the valence state and coordination environment of Zn atoms in Zn−mCN, X-ray absorption fine structure (XAFS) measurements were performed. Fig. 3a shows the Zn K-edge absorption near edge structure (XANES) spectra of Zn−mCN, Zn foil, ZnO and zinc phthalocyanine (ZnPc), respectively, and the absorption edge of Zn−mCN is close to that of ZnO, indicating that the Zn atom valence state is +2, and the results are consistent with the XPS results. Obviously, the absorption edge energy of Zn−mCN is higher than that of ZnPc, which

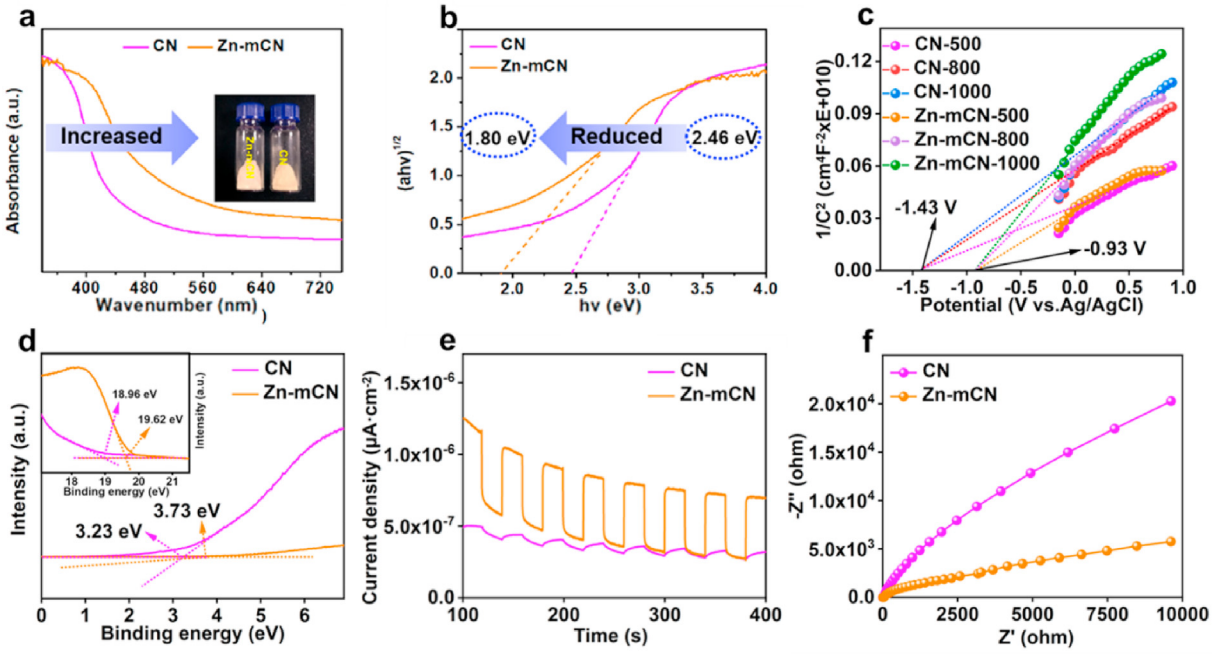

Fig. 4. (a) UV–vis DRS and (b) plot of transformed Kubelka−Munk function versus photo energy for CN and Zn−mCN. Inset in (a) shows a digital photograph of CN and Zn−mCN powders. (c) Mott−Schottky plots of CN and Zn−mCN at frequencies of 500, 800, 1000 Hz in 0.5 mol/L Na_2SO_4 electrolyte. (d) UPS for CN and Zn−mCN. (e) Periodic ON/OFF photocurrent response of CN and Zn−mCN in 0.5 mol/L Na_2SO_4 electrolyte under visible light irradiation ($\lambda > 420$ nm) at 0.5 V vs. Ag/AgCl electrode. (f) EIS of CN and Zn−mCN.

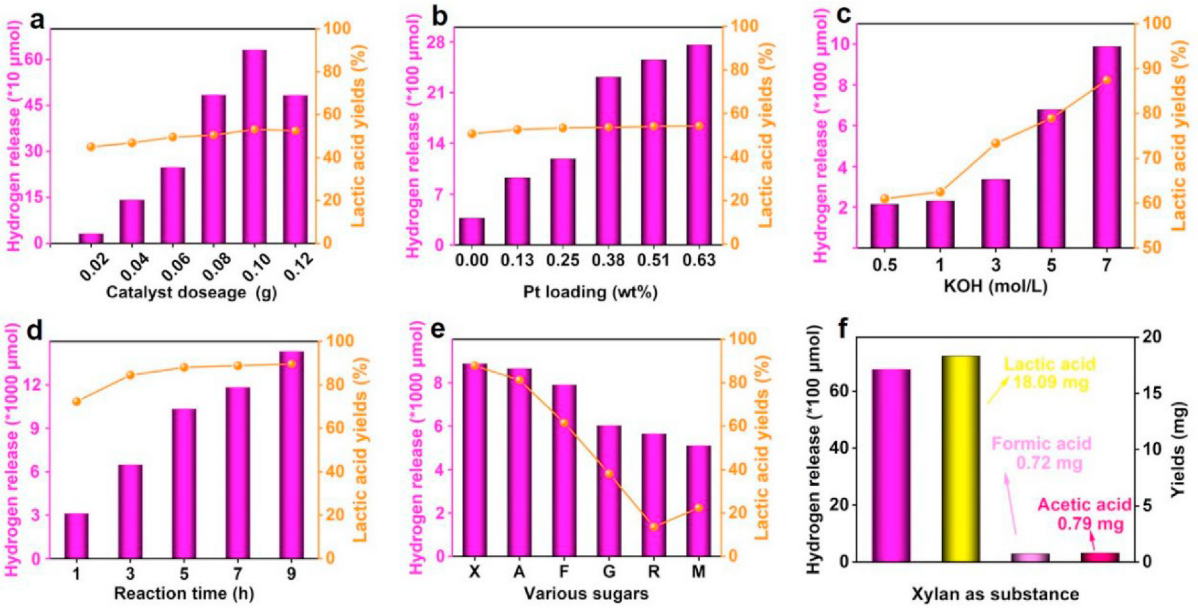

Fig. 5. Effects of different conditions on photocatalytic synchronous biorefinery and water splitting to give lactic acid and hydrogen photocatalyzed by Zn−mCN: (a) Catalyst dosage; (b) Cocatalyst dosage (Pt); (c) KOH concentration; (d) Reaction time; (e) Photocatalytic different sugars conversion and water splitting to lactic acid and hydrogen via Zn−mCN (X: xylose, A: arabinose, F: fructose, G: glucose, R: rhamnose, M: mannose). (f) When xylan as substance for photocatalytic synthesis of value-added chemicals and hydrogen via Zn−mCN.

may be caused by the more N coordination of Zn atom. As shown in Fig. 3b, the main peak of Zn—N between 1 and 2 Å existed in the EXAFS spectrum of Zn−mCN, and no Zn—Zn bond was observed between 2 and 3 Å, indicating that the Zn existed as isolated atoms, which is consistent with the results of AC HAADF-STEM. As we know, XAFS cannot distinguish the bonding types of adjacent elements, such as Zn—C/N/O. In this work, the fitting results were given in Fig. 3c and d and Table S2. Combined with the DFT theoretical calculation, the structure of Zn–N_6 coordination was observed with the Zn—N bond length of 2.12 Å. Also, as compared with the Zn foil, ZnO, and ZnPc, no Zn—Zn signal was presented in the wavelet transform (WT) contour plot of Zn−mCN, further evidencing that the Zn species is atomically dispersed in Zn−mCN (Fig. 3e–h).

3.2. Optical and electrical properties

The loading of Zn single atoms in Zn−mCN has clearly changed the optical properties and light harvesting abilities of carbon nitride. The colour of Zn−mCN powers is faint (the inset in Fig. 4). Fig. 4a and b show the UV–vis diffuse reflectance spectra (DRS) and calculated bandgaps of CN and Zn−mCN, respectively. As compared with CN, Zn−mCN presents a red-shift in the DRS spectrum, resulting in broadened visible light photo-absorption. Accordingly, the bandgap energy is decreased from 2.46 to 1.80 eV. In addition, Mott−Schottky (M−S) plot and ultraviolet photoelectron spectroscopy (UPS) were conducted to investigate the electronic energy of CN and Zn−mCN. It can be seen that the slopes of the M−S curves of CN and Zn−mCN are positive (Fig. 4c), suggesting that they are both n-type semiconductors. Moreover, the flat potential of CN and Zn−mCN is −1.43 V and −0.93 V vs Ag/AgCl, respectively. For n-type semiconductors, CB is 0.2 V more negative than the flat band potential. Thus, the CB of CN and Zn−mCN is −1.63 V vs Ag/AgCl and −1.13 V vs Ag/AgCl, respectively. In general, the reference electrode of CB can be calculated as a normal hydrogen electrode (NHE.) by the Nernst formula ($E_{NHE.} = E_{Ag/AgCl} + 0.197$, pH = 7). Finally, the CB of CN and Zn−mCN can be converted to −1.43 and −0.93 V vs NHE., respectively. The UPS of CN and Zn−mCN is shown in Fig. 4d. The work functions could be obtained by UPS results (Fig. 4d and inset in Fig. 4d), in which that for CN is 2.24 eV (21.2–18.96 eV) and for Zn−mCN is 1.58 eV (21.2–19.62 eV). Furthermore, the valence bands position (VB) of CN and Zn−mCN is identified as 5.47 eV (vs vacuum) and 5.31 eV (vs vacuum), respectively. The VB positions of CN and Zn−mCN are 1.03 and 0.87 eV, respectively. Based on the M−S plots and UPS, the relative band structure scheme of CN and Zn−mCN is shown in Fig. S6. Moreover, photocurrent response of CN and Zn−mCN was also carried out. As displayed in Fig. 4e, Zn−mCN has higher photocurrent density than CN. Moreover, the electrochemical impedance spectroscopy (EIS) Nyquist plots of CN and Zn−mCN are depicted in Fig. 4f. It can be observed that the radius of Nyquist curves for Zn−mCN is smaller than that of CN, indicating that the Zn−mCN is more conductive to the migration of photogenerated carriers. To further investigate charge separation and recombination, photoluminescence (PL) spectra were used to evaluate the efficiency of photoinduced electron (e^-) and hole (h^+). The PL intensity of Zn−mCN is lower than that of CN, suggesting that the charge recombination is interrupted in Zn−mCN (Fig. S7). The phenomenon is similar to the narrow bandgaps of Zn−mCN observed in UV–vis DRS, which can also increase the photocatalytic activity of Zn−mCN [32,33,41].

3.3. Photocatalytic performance of co-production of hydrogen and lactic acid

In the following, the photocatalytic activity of Zn−mCN was investigated by synchronous biorefinery and water splitting in the presence of visible light (10 W). Initially, a series of experiments were carried out to compare the photocatalytic activities of CN and Zn−mCN. As shown in Fig. S8, the hydrogen evolution and lactic acid yield of Zn−mCN were 3.0 times and 1.3 times higher than those of CN, respectively, indicating that the presence of Zn single atoms on CN nanosheet promotes the redox reaction in the system. Then, various catalyst dosages were studied for the redox reaction system. With the Zn−mCN dosage increasing, the yield of hydrogen and lactic acid increased firstly and then decreased (Fig. 5a). One cause may be the xylose adsorbed on the catalyst reduced the activation energy of the entire reaction. Another possibility is related to the low light transmittance with higher catalyst dosage. In addition, the conversion of xylose and the detected by-products (e.g., formic acid, acetic acid) were supplemented in the supplementary materials (Fig. S9).

Next, the effects of Pt (cocatalyst) on the coproduction of lactic acid and hydrogen were also explored. Obviously, as the cocatalyst dosage increased, the hydrogen release significantly raised (Fig. 5b). Meanwhile, the lactic acid yield also showed an increasing trend during these processes, but the change was small (Fig. 5b). The conversion of xylose and the detected by-products were also shown in the supplementary materials (Fig. S10). As we know, pH is an important factor in the photocatalytic redox reaction. Here, only trace yields of lactic acid were observed in the acidic environment (0.5 mol/L HCl) and neutral (deionized water), but 54.2% yield of lactic acid and 2758.4 μmol hydrogen were detected in KOH solution (0.5 mol/L), suggesting that alkaline environment is favoured for the production of lactic acid and hydrogen via Zn−mCN photocatalysis. Further studies indicated that the yields of lactic acid and hydrogen also increased with the KOH concentration increasing, and 87.4% yield of lactic acid and 9882.1 μmol hydrogen were achieved in the 30 mL KOH (7.0 mol/L) solution with 300 mg xylose and 100 mg catalyst for 5 h (Fig. 5c). Similarly, the conversion of xylose and the yields of acetic acid and formic acid were also provided in the supplementary materials (Fig. S11). Subsequently, the effects of the irradiation time of visible light (10 W) on the photocatalytic synchronous biorefinery and water splitting were investigated. As shown in Fig. 5d, the hydrogen release significantly increased from 3128.1 μmol to 14308 μmol as the irradiation time increased from 1 h to 9 h, and meanwhile, the yield and selectivity of lactic acid reached 89.6% and 91.0%, respectively. The conversions of xylose and the by-products (e.g., acetic acid, formic acid) were also detected during these processes and presented in supplementary materials (Fig. S12). The turnover frequency (TOF) of Zn was measured in order to better study the efficiency of the utilization of Zn single atoms. The TOF of Zn−mCN is measured to be 65.9 h^{-1}. According to the above analysis, the Zn−mCN is an excellent photocatalyst for photocatalytic synchronous biorefinery and water splitting to give lactic acid and hydrogen.

To explore the effect of Zn loading on hydrogen evolution and lactic acid production, a series of experiments with different Zn loading were performed. As shown in Fig. S13, the hydrogen release increased with the Zn loading of Zn−mCN. The yield of lactic acid first increased with the Zn loading of Zn−mCN and then decreased. Meanwhile, as we know, lactic acid is also a sacrificial agent. With the progress of the reaction, lactic acid is generated and consumed in the reaction system, which can be the reason for the above phenomenon. Furthermore, to verify whether the redox reaction is related to visible light, the reaction systems were reacted under dark and visible light irradiation, respectively. As shown in Fig. S14, no hydrogen was obtained under dark condition. The lactic acid yield in the visible light irradiation system increased by nearly 40% as compared with dark condition. The xylose conversion is only 65% under dark and reached 98% under the visible light irradiation. This result shows that visible light plays an important role in biomass conversion. To verify the importance of Zn single atoms system in this study, a series of experiments were performed. Firstly, the Zn particles anchored on the CN were prepared without HCl addition, and other preparation processes were the same as those of Zn−mCN. Subsequently, 300 mg of xylose, 20 mg of photocatalysts and the same addition of $H_2PtCl_6{\cdot}6H_2O$ were added into 30 mL of KOH solution. These two systems were sonicated for 5 min and then filled with Ar (101 kPa). Finally, the obtained systems were performed at 30 °C for 2 h in the presence of visible light (10 W). The results indicated that the hydrogen evolution (5364.44 μmol g^{-1} h^{-1}) and the lactic acid yield (59.03%) of Zn particles system were far lower than those of Zn single atoms system (hydrogen evolution: 10142.26 μmol g^{-1} h^{-1}, lactic acid yield: 87.6%), suggesting the promoting effect of Zn single atoms for this reaction system.

3.4. Photocatalytic biomass-derived feedstocks to co-produce lactic acid and hydrogen via Zn−mCN photocatalysis

As we know, the universality of the catalyst is also an important parameter that affects its utilization. Here, various biomass-derived pentoses (e.g., xylose, arabinose) and hexoses (e.g., glucose, fructose, rhamnose, mannose) were investigated for photocatalytic synchronous biorefinery and water splitting to give lactic acid and hydrogen. All the systems exhibited excellent photocatalytic redox activity for hydrogen release and sugar oxidation (Fig. 5e). Interestingly, the hydrogen release rate of pentose systems was higher than that of hexoses, and the selectivity of lactic acid also showed the same change trend (Fig. 5e), but the conversion of xylose was similar (Fig. S15). Likewise, a certain amount of acetic acid and formic acid were also detected during these processes. Furthermore, when the small molecular (e.g., biomass-derived sugars) was replaced by macromolecular substrate (xylan), the hydrogen release rate reached 13533.8 μmol g^{-1} h^{-1} while the lactic acid yield achieved 18.09 mg during this process, and 0.72 mg of formic acid as well as 0.79 mg of acetic acid were also detected (Fig. 5f). These results indicated that the system is suitable for biomass reaction systems with different molecular masses.

3.5. Recycling stability of Zn−mCN on co-production of hydrogen and lactic acid

Furthermore, the reusability of Zn−mCN was also explored in the presence of 30 mL of KOH (7.0 mol/L) with 300 mg of xylose and 0.3 mL of $H_2PtCl_6{\cdot}6H_2O$ (6.5 mmol/L) as well as 100 mg of Zn−mCN at room temperature for 5 h irradiated by visible light (10 W). As shown in Fig. S16, the retained hydrogen release rate, lactic acid yield and xylose conversion were about 78.1%, 90.8% and 92.3% after being used five times, indicating that Zn−mCN has excellent reusability.

3.6. Comparison of photocatalytic activity of Zn−mCN and different reported catalysts

In order to better understand the reaction system of the catalyst, the effects of Zn−mCN on the lactic acid production were compared to those of functional carbon nitride photocatalysts reported previously. Interestingly, the reaction temperature of the Zn−mCN photocatalytic system is lower than that of the reported systems, and the yield of lactic acid is higher than that of them (Table S3) [33,42–44]. For hydrogen generation, as compared with the most of reported literature, Zn−mCN shows excellent photocatalytic performance (Table S4) [45–49]. Generally, although the single system displays good activity in hydrogen release or lactic acid synthesis, co-production of hydrogen via reduction half-reaction and lactic acid production via oxidation half-reaction remains a desirable, yet challenging goal in one system. Interestingly, in the Zn−mCN photocatalytic system, the lactic acid and hydrogen were all produced via the oxidation and reduction half-reaction, respectively. Obviously, the Zn−mCN system has excellent environmental and economic benefits.

3.7. ESR characterization and effects of various oxidation active species on co-production of hydrogen and lactic acid

To further investigate the effects of various oxidation active species on the photocatalytic synchronous biorefinery and water splitting, electron spin-resonance (ESR) measurements and poisoning experiments were performed. As shown in Fig. S17a, the signal of TEMPO exhibits triple peaks with the intensity of 1:1:1. Once the e^- was generated, the TEMPO−e^- formed. The signal intensity of TEMPO decreased as the irradiation time increased. The change of TEMPO signals in the Zn−mCN system is consistent with that of CN (Fig. S17b). Additionally, the signal intensity of TEMPO in the Zn−mCN system is lower when compared to that of CN, suggesting that more e^- was generated in the Zn−mCN system (Fig. 6a). As h^+ is always paired with e^-, the change of h^+ signals showed the same trend as that of e^- (Figs. 6b and S18). The DMPO and $\cdot O_2^-$ have no signals in the CN or Zn−mCN system in the dark conditions. When the irradiation was applied, an adduct of DMPO/$\cdot O_2^-$ was formed,

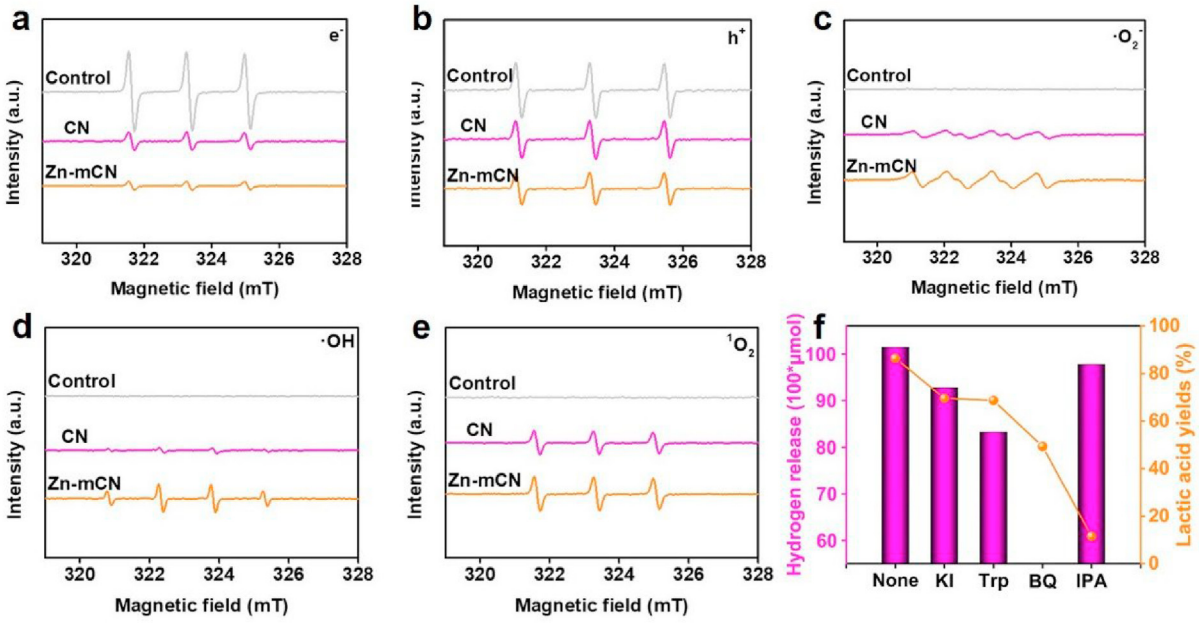

Fig. 6. TEMPO ESR spin-labeling for e^- (a) and h^+ (b) of CN and Zn−mCN in the same conditions. DMPO ESR spin-labeling for $\cdot O_2^-$ (c) and ·OH (d) of CN and Zn−mCN in the same conditions. (e) TEMPO ESR spin-labeling for $^1O_2$ of CN and Zn−mCN in the same conditions. (f) Effects of different oxidation active species on photocatalytic synchronous xylose conversion and water splitting to give lactic acid and hydrogen via Zn−mCN.

along with the quadruple signal peaks with intensity of 1:1:1:1. With the increase of illumination time, the signal strengthened gradually (Fig. S19). These results indicated that the $\cdot O_2^-$ was generated in the system under the irradiation. The longer the reaction time was, the more the $\cdot O_2^-$ was generated. Under the same conditions, the signal from Zn−mCN was stronger than that of CN (Fig. 6c), suggesting that higher amount of $\cdot O_2^-$ can be produced in Zn−mCN than in CN. DMPO was used as ESR spin-labeling for ·OH, and the adduct of DMPO/·OH was generated under the irradiation. The changing trend of DMPO/·OH signals was similar to that of DMPO/$\cdot O_2^-$, except that the intensity of quadruple signal peaks of DMPO/·OH is 1:2:2:1 (Figs. 6d and S20). $^1O_2$ is a special form in existence, which is strongly selective. TEMPONE was used as ESR spin-labeling to detect $^1O_2$. No signal was observed in the dark conditions for CN or Zn−mCN, as well as the systems irradiated without photocatalysts (Fig. S21). Once the irradiation was applied to the system catalyzed with CN or Zn−mCN, a triple signal peak with intensity of 1:1:1 was presented (Fig. S21), indicating that $^1O_2$ was generated in the two systems. As the irradiation time increased, the signals intensity strengthened, due to the accumulation of $^1O_2$. Additionally, the detected $^1O_2$ signal in the CN system was weaker than that in the Zn−mCN system (Fig. 6e), suggesting that the loading of Zn single atoms in Zn−mCN is beneficial to the generation of $^1O_2$.

As we know, when the visible is irradiated on the surface of photocatalysts, the absorbed photons can be excited. Then, e^-−h^+ pairs are formed and participate in the generation of oxidation active species, and e^- can be reacted with O_2 to give $\cdot O_2^-$; the $^1O_2$ can be produced via $\cdot O_2^-$ reacted with h^+. In addition, h^+ can also generate ·OH via the combination with OH^-. In this work, the above active species were all generated in the Zn−mCN photocatalytic system. To investigate the effects of various oxidative active species on the reaction, a series of poisoning experiments were performed. As shown in Fig. 6f, when specific sacrificial agents (e.g., IPA, BQ, KI, and Trp) were added into the reaction systems, respectively, the yields of lactic acid and hydrogen release rate were all decreased as compared to those of the systems without sacrificial agents (Fig. 6f). These results suggested that the h^+, $^1O_2$, $\cdot O_2^-$ and ·OH species all play important roles in the synthesis of lactic acid from xylose and production of hydrogen via water splitting photocatalyzed by Zn−mCN.

3.8. Possible reaction mechanism of photocatalytic co-production of hydrogen and lactic acid via Zn-mCN

Based on the above results, a possible reaction mechanism of simultaneous photocatalytic water splitting and biorefinery was proposed (Fig. S22). Firstly, Zn−mCN absorbed photons and became excited to generate e^-−h^+ pairs. Next, the photo-generated e^- migrated from the CB of Zn−mCN to Pt nanoparticles, and then the proton combined with e^- to generate H_2 in the reduction half-reaction. Meanwhile, $\cdot O_2^-$ was produced by the reaction between e^- and O_2 [50]. $^1O_2$ was formed by the combination of $\cdot O_2^-$ and h^+ [51]. In addition, h^+ reacted with OH^- to generate ·OH [52]. According to the previous reports [44,53–55] and the experimental results, in the oxidation half-reaction, xylose was converted to intermediate I via isomerization. Subsequently, intermediate II was produced by the isomerization of intermediate I. Meanwhile, glyceradehyde and oxalic acid were generated from intermediate I via retro−aldol mechanism, and then glyceradehyde was converted to lactic acid. Furthermore, on the one hand, the xylose and intermediate I were converted to intermediate III and acetic acid via α-oxidation. On the other hand, the intermediate III and oxalic acid were obtained from intermediate I and intermediate II via β-oxidation. In addition, formic acid was also produced from oxalic acid. Due to the high yield, lactic acid was regarded as the primary product.

4. Conclusions

To summarize, we reported a CCW strategy to prepare Zn−mCN photocatalyst with high dispersion of single Zn atoms. The loading of single Zn atoms was adjustable in the structure of Zn−mCN. Widened adsorption to visible light and lowered PL intensity were achieved by the Zn−mCN photocatalysts as compared with CN. Zn−mCN showed excellent photocatalytic redox activity for synchronous biorefinery and water splitting to co-product lactic acid (selectivity up to 91.0%) and hydrogen (up to 15898.8 μmol g^{-1} h^{-1}). This system has excellent photocatalytic redox activity for different biomass-derived monosaccharides and macromolecular xylan in co-production of lactic acid and hydrogen , in which xylan was used as substance, and the hydrogen release and lactic acid yield reached 13533.8 μmol g^{-1} h^{-1} and 18.09 mg/300 mg,

respectively. Amongst them, for monosaccharides, the activity of pentoses is obviously better than that of hexoses. For lactic acid production, ·OH plays an important role while $\cdot O_2^-$ significantly affects the hydrogen release. This work realized full utilization of whole redox reaction and provided a novel strategy for efficient and concomitant production of hydrogen and value-added chemicals from biomass-derived feedstocks aqueous solutions via photocatalysis.

Declaration of competing interest

The authors declare that they have no known competing financial interests or personal relationships that could have appeared to influence the work reported in this paper.

Acknowledgments

This work was supported by the National Natural Science Foundation of China (No. 22008018), China Postdoctoral Science Foundation (No. 2020M670716), the Natural Science Foundation of Liaoning Province, China (No. 2020-MS-272), the Foundation of Guangxi Key Laboratory of Clean Pulp & Papermaking and Pollution Control, College of Light Industry and Food Engineering, Guangxi University (No. 2021KF08), Dalian City Outstanding Talent Project (No. 2019RD13), the Start-up Fund for Doctoral Research of Dalian Polytechnic University (No. 2020–07), the Foundation of State Key Laboratory of Biobased Material and Green Papermaking, Qilu University of Technology, Shandong Academy of Sciences (No. KF201914), and the Foundation of Key Laboratory of State Forestry and Grassland Administration for Plant Fiber Functional Materials (No. 2020KFJJ06). We also thank to the Shiyanjia Lab (http://www.shiyanjia.com) for the XPS analysis.

Appendix A. Supplementary data

Supplementary data to this article can be found online at https://doi.org/10.1016/j.apmate.2022.100058.

References

[1] E. Lam, E. Reisner, A TiO_2-Co(terpyridine)(2) photocatalyst for the selective oxidation of cellulose to formate coupled to the reduction of CO_2 to syngas, Angew. Chem. Int. Ed. 60 (2021) 23306–23312.
[2] X.Y. Bai, Q.D. Hou, H.L. Qian, Y.F. Nie, T.L. Xia, R.T. Lai, G.J. Yu, M.L.U. Rehman, H.J. Xie, M.T. Ju, Selective oxidation of glucose to gluconic acid and glucaric acid with chlorin e6 modified carbon nitride as metal-free photocatalyst, Appl. Catal. B Environ. 303 (2022), 120895.
[3] Z.L. Dou, Z. Zhang, H.R. Zhou, M. Wang, Photocatalytic upgrading of lignin oil to diesel precursors and hydrogen, Angew. Chem. Int. Ed. 60 (2021) 16399–16403.
[4] H. Zhao, C.F. Li, X.T. Yu, N. Zhong, Z.Y. Hu, Y. Li, S. Larter, M.G. Kibria, J.G. Hu, Mechanistic understanding of cellulose beta-1,4-glycosidic cleavage via photocatalysis, Appl. Catal. B Environ. 302 (2022), 120872.
[5] M. Zhang, Z.H. Yu, J. Xiong, R. Zhang, X.Z. Liu, X.B. Lu, One-step hydrothermal synthesis of $Cd_xIn_yS_{(x+1.5y)}$ for photocatalytic oxidation of biomass-derived 5-hydroxymethylfurfural to 2, 5-diformyl-furan under ambient conditions, Appl. Catal. B Environ. 300 (2022), 120738.
[6] C. Li, J. Li, L. Qin, P.P. Yang, D.G. Vlachos, Recent advances in the photocatalytic conversion of biomass-derived furanic compounds, ACS Catal. 11 (2021) 11336–11359.
[7] N.C. Luo, T. Montini, J. Zhang, P. Fornasiero, E. Fonda, T.T. Hou, W. Nie, J.M. Lu, J.X. Liu, M. Heggen, L. Lin, C.T. Ma, M. Wang, F.T. Fan, S.Y. Jin, F. Wang, Visible-light-driven coproduction of diesel precursors and hydrogen from lignocellulose-derived methylfurans, Nat. Energy 4 (2019) 575.
[8] Z. Zhang, M. Wang, H.R. Zhou, F. Wang, Surface sulfate ion on CdS catalyst enhances syngas generation from biopolyols, J. Am. Chem. Soc. 143 (2021) 6533–6541.
[9] D.W. Wakerley, M.F. Kuehnel, K.L. Orchard, K.H. Ly, T.E. Rosser, E. Reisner, Solar-driven reforming of lignocellulose to H_2 with a CdS/CdO_x photocatalyst, Nat. Energy 2 (2017) 17021.
[10] G. Zhang, C. Ni, X. H, A. Welgamage, L.A. Lawton, P. Robertson, J. Irvine, Simultaneous cellulose conversion and hydrogen production assisted by cellulose decomposition under uv-light photocatalysis, Chem. Commun. 52 (2016) 1673–1676.
[11] L.Z. Wang, R. Tang, A. Kheradmand, Y.J. Jiang, H. Wang, W.J. Yang, Z.B. Chen, X. Zhong, S.P. Ringer, X.Z. Liao, W.B. Liang, J. Huang, Enhanced solar-driven benzaldehyde oxidation with simultaneous hydrogen production on Pt single-atom catalyst, Appl. Catal. B Environ. 300 (2022), 120738.
[12] L. Cheng, X.Y. Yue, L.X. Wang, D.N. Zhang, P. Zhang, J.J. Fan, Q.J. Xiang, Dual-single-atom tailoring with bifunctional integration for high-performance CO_2 photoreduction, Adv. Mater. 33 (2021), 2105135.
[13] X. Ma, H. Liu, W.J. Yang, G.Y. Mao, L.R. Zheng, H.L. Jiang, Modulating coordination environment of single-atom catalysts and their proximity to photosensitive units for boosting MOF photocatalysis, J. Am. Chem. Soc. 143 (2021) 12220–12229.
[14] Z.Y. Chen, S.Q. Wu, J.Y. Ma, S. Mine, T. Toyao, M. Matsuoka, L.Z. Wang, J.L. Zhang, Non-oxidative coupling of methane: N-type doping of niobium single atoms in TiO_2-SiO_2 induces electron localization, Angew. Chem. Int. Ed. 60 (2021) 11901–11909.
[15] H.C. Hu, W.H. Guan, Y.F. Xu, X.C. Wang, L.Z. Wu, M. Chen, Q.X. Zhong, Y. Xu, Y.Y. Li, T.K. Sham, X.H. Zhang, L. Wang, M.H. Gao, Q. Zhang, Construction of single-atom platinum catalysts enabled by $CsPbBr_3$ nanocrystals, ACS Nano 15 (2021) 13129–13139.
[16] M.P. Kou, W. Liu, Y.Y. Wang, J.D. Huang, Y.L. Chen, Y. Zhou, Y. Chen, M.Z. Ma, K. Lei, H.Q. Xie, P.K. Wong, L.Q. Ye, Photocatalytic CO_2 conversion over single-atom MoN_2 sites of covalent organic framework, Appl. Catal. B Environ. 291 (2021), 120146.
[17] D.Q. Liu, A. Barbar, T. Najam, M.S. Javed, J. Shen, P. Tsiakaras, X.K. Cai, Single noble metal atoms doped 2D materials for catalysis, Appl. Catal. B Environ. 297 (2021), 120389.
[18] X.D. Xiao, Y.T. Gao, L.P. Zhang, J.C. Zhang, Q. Zhang, Q. Li, H.L. Bao, J. Zhou, S. Miao, N. Chen, J.Q. Wang, B.J. Jiang, C.G. Tian, H.G. Fu, A promoted charge separation/transfer system from Cu single atoms and C_3N_4 layers for efficient photocatalysis, Adv. Mater. 32 (2020), 2003082.
[19] G. Wang, R. Huang, J.W. Zhang, J.J. Mao, D.S. Wang, Y.D. Li, Synergistic modulation of the separation of photo-generated carriers via engineering of dual atomic sites for promoting photocatalytic performance, Adv. Mater. 33 (2021), 2105904.
[20] G. Wang, C.T. He, R. Huang, J.J. Mao, D.S. Wang, Y.D. Li, Photoinduction of Cu single atoms decorated on UiO-66-NH_2 for enhanced photocatalytic reduction of CO_2 to liquid fuels, J. Am. Chem. Soc. 142 (2020) 19339–19345.
[21] P.X. Liu, Y. Zhao, R.X. Qin, S.G. Mo, G.X. Chen, L. Gu, D.M. Chevrier, P. Zhang, Q. Guo, D.D. Zang, B.H. Wu, G. Fu, N.F. Zheng, Photochemical route for synthesizing atomically dispersed palladium catalysts, Science 352 (2016) 797–801.
[22] A.J. Han, W.X. Chen, S.L. Zhang, M.L. Zhang, Y.H. Han, J. Zhang, S.F. Ji, L.R. Zheng, Y. Wang, L. Gu, C. Chen, Q. Peng, D.S. Wang, Y.D. Li, A polymer encapsulation strategy to synthesize porous nitrogen-doped carbon-nanosphere-supported metal isolated-single-atomic-site catalysts, Adv. Mater. 30 (2018), 1706508.
[23] J. Li, S.G. Chen, N. Yang, M.M. Deng, S. Ibraheem, J.H. Deng, J. Li, L. Li, Z.D. Wei, Ultrahigh-loading zinc single-atom catalyst for highly efficient oxygen reduction in both acidic and alkaline media, Angew. Chem. Int. Ed. 58 (2019) 7035–7039.
[24] P. Song, M. Luo, X.Z. Liu, W. Xing, W.L. Xu, Z. Jiang, L. Gu, Zn single atom catalyst for highly efficient oxygen reduction reaction, Adv. Funct. Mater. 27 (2017), 1700802.
[25] S. Xu, P. Zhou, Z.H. Zhang, C.J. Yang, B.G. Zhang, K.J. Deng, S. Bottle, H.Y. Zhu, Selective oxidation of 5-hydroxymethylfurfural to 2,5-furandicarboxylic acid using O_2 and a photocatalyst of Co-thioporphyrazine bonded to g-C_3N_4, J. Am. Chem. Soc. 139 (2017) 14775–14782.
[26] X.X. Jia, J.W. Zhao, Y.J. Lv, X.L. Fu, Y.J. Jian, W.Q. Zhang, Y.Y. Wang, H.M. Sun, X.X. Wang, J.L. Long, P. Yang, Q. Gu, Z.W. Gao, Low-crystalline PdCu alloy on large-area ultrathin 2D carbon nitride nanosheets for efficient photocatalytic Suzuki coupling, Appl. Catal. B Environ. 300 (2022), 120756.
[27] B. Ma, G. Chen, C. Fave, L.J. Chen, R. Kuriki, K. Maeda, O. Ishitani, T.C. Lau, J. Bonin, R.M. Obert, Efficient visible-light-driven CO_2 reduction by a cobalt molecular catalyst covalently linked to mesoporous carbon nitride, J. Am. Chem. Soc. 142 (2020) 6188–6195.
[28] J.P. Hong, B. Wang, G.Q. Xiao, N. Wang, Y.H. Zhang, A.Y. Khodakov, J.L. Li, Tuning the metal-support interaction and enhancing the stability of titania-supported cobalt fischer-tropsch catalysts via carbon nitride coating, ACS Catal. 10 (2020) 5554–5566.
[29] J.L. Ma, Y.C. Li, D.N. Jin, X.P. Yang, G.J. Jiao, K.N. Liu, S.F. Sun, J.H. Zhou, R.C. Sun, Reasonable regulation of carbon/n(ride ratio in carbon nitride for efficient photocatalytic reforming of biomass-derived feedstocks to lactic acid, Appl. Catal. B Environ. 299 (2021), 120698.
[30] J.L. Ma, K.N. Liu, X.P. Yang, D.N. Jin, Y.C. Li, G.J. Jiao, J.H. Zhou, R.C. Sun, Recent advances and challenges in photoreforming of biomass-derived feedstocks into hydrogen, biofuels, or chemicals by using functional carbon nitride Photocatalysts, ChemSusChem 14 (2021) 4903–4922.
[31] J.L. Ma, D.N. Jin, X.P. Yang, S.L. Sun, J.H. Zhou, R.C. Sun, Phosphorus-doped carbon nitride with grafted sulfonic acid groups for efficient photocatalytic synthesis of xylonic acid, Green Chem. 23 (2021) 4150–4160.
[32] J.L. Ma, D.N. Jin, Y.C. Li, D.Q. Xiao, G.J. Jiao, Q. Liu, Y.Z. Guo, L.P. Xiao, X.H. Chen, X.Z. Li, J.H. Zhou, R.C. Sun, Photocatalytic conversion of biomass-based monosaccharides to lactic acid by ultrathin porous oxygen doped carbon nitride, Appl. Catal. B Environ. 283 (2021), 119520.
[33] J.L. Ma, Y.C. Li, D.N. Jin, Z. Ali, G.J. Jiao, J.Q. Zhang, S. Wang, R.C. Sun, Functional B@*m*CN-assisted photocatalytic oxidation of biomass-derived pentoses and hexoses to lactic acid, Green Chem. 22 (2020) 6384–6392.
[34] H.J. Yu, R. Shi, Y.X. Zhao, T. Bian, Y.F. Zhao, C. Zhou, G.I.N. Waterhouse, L.Z. Wu, C.H. Tung, T.R. Zhang, Alkali-assisted synthesis of nitrogen deficient graphitic

carbon nitride with tunable band structures for efficient visible-light-driven hydrogen evolution, Adv. Mater. 29 (2017), 1605148.
[35] G.C. Lei, W.T. Zhao, L.J. Shen, S.J. Liang, C.T. Au, L.L. Jiang, Isolated iron sites embedded in graphitic carbon nitride (g-C_3N_4) for efficient oxidative desulfurization, Appl. Catal. B Environ. 267 (2020), 118663.
[36] Y.Z. Zhang, J.W. Shi, Z.X. Huang, X.J. Guan, S.C. Zong, C. Cheng, B.T. Zheng, L.J. Guo, Synchronous construction of CoS_2 in-situ loading and S doping for g-C_3N_4: enhanced photocatalytic H_2 evolution activity and mechanism insight, Chem. Eng. J. 401 (2020), 126135.
[37] G.C. Wang, T. Zhang, W.W. Yu, R. Si, Y.F. Liu, Z.K. Zhao, Modulating location of single copper atoms in polymeric carbon nitride for enhanced photoredox catalysis, ACS Catal. 10 (2020) 5715–5722.
[38] J. Li, B.J. Huang, Q. Guo, S. Guo, Z.K. Peng, J. Liu, Q.Y. Tian, Y.P. Yang, Q. Xu, Z.Y. Liu, B. Liu, Van der Waals heterojunction for selective visible-light-driven photocatalytic CO_2 reduction, Appl. Catal. B Environ. 284 (2021), 119733.
[39] G.M. Liu, Y. Huang, H.Q. Lv, H. Wang, Y.B. Zeng, M.Z. Yuan, Q.G. Meng, C.Y. Wang, Confining single-atom Pd on g-C_3N_4 with carbon vacancies towards enhanced photocatalytic NO conversion, Appl. Catal. B Environ. 284 (2021), 119683.
[40] Q. Wang, T. Ina, W.T. Chen, L. Shang, F.F. Sun, S.H. Wei, D. Sun-Waterhouse, D.S.G. Telfer, T.R. Zhang, G.I.N. Waterhouse, Evolution of Zn(II) single atom catalyst sites during the pyrolysis-induced transformation of ZIF-8 to N-doped carbons, Sci. Bull. 65 (2020) 1743–1751.
[41] X.B. Li, S.T.A.G. Melissenp, T. Le Bahers, P. Sautet, A.F. Masters, Shining light on carbon nitrides: leveraging temperature to understand optical gap variations, Chem. Mater. 30 (2018) 4253–4262.
[42] Y.C. Li, J.L. Ma, D.N. Jin, G.J. Jiao, X.P. Yang, K.N. Liu, J.H. Zhou, R.C. Sun, Copper oxide functionalized chitosan hybrid hydrogels for highly efficient photocatalytic-reforming of biomass-based monosaccharides to lactic acid, Appl. Catal. B Environ. 291 (2021), 120123.
[43] X.P. Yang, J.L. Ma, S.F. Sun, Z.D. Liu, R.C. Sun, K/O co-doping and introduction of cyano groups in polymeric carbon nitride towards efficient simultaneous solar photocatalytic water splitting and biorefineries, Green Chem. 24 (2022) 2104–2113.
[44] K.N. Liu, J.L. Ma, X.P. Yang, Z.D. Liu, X.Z. Li, J.Q. Zhang, R. Cui, R.C. Sun, Phosphorus/oxygen co-doping in hollow-tube-shaped carbon nitride for efficient simultaneous visible-light-driven water splitting and biorefinery, Chem. Eng. J. 437 (2022), 135232.
[45] Y.X. Zhang, Q.X. Cao, X.L. Wu, Y.H. Xiao, A.Y. Meng, Q.T. Zhang, Y.X. Yu, W.D. Zhang, Efficient photocatalytic H_2 evolution and α-methylation of ketones from copper complex modified polymeric carbon nitride, Chem. Eng. J. 427 (2022), 132042.
[46] C. Cheng, C.L. Dong, J.W. Shi, L.H. Mao, Y.C. Huang, X. Kang, S.C. Zong, S.H. Shen, Regulation on polymerization degree and surface feature in graphitic carbon nitride towards efficient photocatalytic H_2 evolution under visible-light irradiation, J. Mater. Sci. Technol. 98 (2022) 160–168.
[47] Y.L. Chen, F.Y. Su, H.Q. Xie, R.P. Wang, C.H. Ding, J.D. Huang, Y.X. Xu, L.Q. Ye, One-step construction of S-scheme heterojunctions of N-doped MoS_2 and S-doped g-C_3N_4 for enhanced photocatalytic hydrogen evolution, Chem. Eng. J. 404 (2021), 126498.
[48] Z.H. Liao, C.X. Li, Z. Shu, J. Zhou, T.T. Li, W.B. Wang, Z.L. Zhao, L.N. Xu, L.L. Shi, L.L. Feng, K-Na co-doping in crystalline polymeric carbon nitride for highly improved photocatalytic hydrogen evolution, Int. J. Hydrogen Energy 46 (2021) 26318–26328.
[49] Q. Li, L.M. Zhang, J.N. Liu, J. Zhou, Y.Q. Jiao, X.D. Xiao, C. Zhao, Y. Zhou, S. Ye, B.J. Jiang, J. Liu, Porous carbon nitride thin strip: Precise carbon doping regulating delocalized π-electron induces elevated photocatalytic hydrogen evolution, Small 17 (2021), 2006622.
[50] S.H. Zhang, J.T. Lv, R.X. Han, Z. Wang, P. Christie, S.Z. Zhang, Sustained production of superoxide radicals by manganese oxides under ambient dark conditions, Water Res. 196 (2021), 117034.
[51] R. Ossola, O.M. Jönsson, K. Moor, K. McNeill, Singlet oxygen quantum yields in environmental waters, Chem. Rev. 121 (2021) 4100–4146.
[52] G. Feng, P. Cheng, W.F. Yan, M. Boronat, X. Li, J.H. Su, J.Y. Wang, Y. Li, A. Corma, J.H. Yu, Accelerated crystallization of zeolites via hydroxyl free radicals, Science 351 (2016) 1188–1191.
[53] L. Yang, J. Su, S. Carl, J.G. Lynam, X.K. Yang, H.F. Lin, Catalytic conversion of hemicellulosic biomass to lactic acid in pH neutral aqueous phase media, Appl. Catal. B Environ. 162 (2015) 149–157.
[54] F. de Clippel, M. Dusselier, R. Van Rompaey, P. Vanelderen, J. Dijkmans, E. Makshina, L. Giebeler, S. Oswald, G.V. Baron, J.F.M. Denayer, P.P. Pescarmona, P.A. Jacobs, B.F. Sels, Fast and selective sugar conversion to alkyl lactate and lactic acid with bifunctional carbon-silica catalysts, J. Am. Chem. Soc. 134 (2012) 10089–10101.
[55] M. Spangsberg holm, S. Saravamurugan, E. Taarning, Conversion of sugars to lactic acid derivatives using heterogeneous zeotype catalysts, Science 328 (2010) 602–605.